Materials Advances

ROYAL SOCIETY OF CHEMISTRY

PAPER

View Article Online
View Journal | View Issue

Check for updates

Cite this: *Mater. Adv.*, 2025, 6, 2811

Design and synthesis of PANI/GO/MoS_2 nanocomposites *via* oxidative polymerization for efficient photocatalytic applications: organic pollutant degradation and hydrogen generation†

Pritam Hait,[a] Rajeev Mehta[b] and Soumen Basu *[a]

This study focused on preparing a ternary nanocomposite (PANI/GO/MoS_2) using an oxidative polymerization technique. The composite incorporated polyaniline (PANI), graphene oxide (GO), and molybdenum disulfide (MoS_2) in different weight ratios. Comprehensive characterization studies were performed including UV-vis-DRS, PL, XRD, XPS, BET, and EDS to evaluate the material's crystallinity, purity, porosity, and optical properties. FESEM imaging revealed the porous nature of PANI, the exfoliated structure of GO, and the nanosphere morphology of MoS_2 (35–55 nm in diameter). This composite was tested for its effectiveness in degrading methyl orange (MO) dye and generating green hydrogen *via* visible-light-driven water splitting. Within 120 minutes, it achieved around 81.23% detoxification and 99% removal of MO dye. The degradation process adhered to first-order kinetics with a rate constant 7.1 times higher than that of pure PANI, 22 times higher than that of GO, 6.35 times higher than that of MoS_2, and 9.26 times greater than that of the commercial TiO_2-P25 photocatalyst, indicating strong synergy among the components. The study also examined the impact of various reaction parameters like pH, illumination area, catalyst dosage, and scavengers on the degradation process. The reusability of the photocatalyst was assessed over six cycles, maintaining 80% stability, as confirmed by XRD analysis. GC-MS identified the intermediates and final degradation products. The nanocomposite achieved hydrogen production with an apparent quantum efficiency (AQE) of 26% using CH_3OH as a sacrificial agent, and AQEs of 22%, 19%, and 15% under acidic, basic, and neutral conditions, respectively. This research highlights the potential of ternary nanocomposites for diverse applications beyond dye degradation, including various solar-driven technologies.

Received 16th December 2024,
Accepted 10th March 2025

DOI: 10.1039/d4ma01249f

rsc.li/materials-advances

Open Access Article. Published on 13 March 2025. Downloaded on 2/2/2026 9:34:04 AM.
This article is licensed under a Creative Commons Attribution-NonCommercial 3.0 Unported Licence.

1. Introduction

Semiconductor-based photocatalysis has gained prominence for solar fuel production and pollutant degradation, driven by urgent energy and environmental challenges.[1–3] The discharge of dye waste from industries like paper, leather, and nylon production significantly affects aquatic life by causing water pollution. Reducing the coloration of these dyes is a crucial step in wastewater treatment prior to environmental discharge due to their synthetic origin, intricate chemical composition, and potential toxicity, as well as their carcinogenic or explosive properties.[4] The rapid exhaustion of fossil fuels like coal, natural gas, and oil, along with rising political and environmental concerns, has heightened the need for renewable energy from sustainable sources for long-term solutions.[5] This has led to numerous efforts in investigating innovative approaches to advancing renewable energy technologies. In recent years, transforming solar energy into chemical energy as solar fuels like hydrogen, methanol, and methane has emerged as a promising solution.[6] This approach aims to lessen our heavy reliance on depleting fossil resources and address future energy and environmental challenges. Hydrogen (H_2) plays a vital role as a superior energy carrier essential for promoting a low-carbon emission economy. While hydrogen (H_2) may pose challenges related to safe transportation, it possesses numerous significant advantages: (i) in addition to its environmental friendliness, hydrogen (H_2) is also non-toxic, setting it apart from most other fuel sources; (ii) with its abundant resources, hydrogen

[a] *Department of Chemistry and Biochemistry, TIET-Virginia Tech Center of Excellence in Emerging Materials, Thapar Institute of Engineering & Technology, Patiala, 147004, India. E-mail: soumen.basu@thapar.edu*
[b] *Department of Chemical Engineering, TIET-Virginia Tech Center of Excellence in Emerging Materials, Thapar Institute of Engineering & Technology, Patiala, 147004, India*

† Electronic supplementary information (ESI) available: Chemical details, information about the instruments, EDS, FTIR, BET-BJH plots, EIS analysis, Mott–Schottky plot, GC-TCD results of hydrogen generation, GC-MS data, and a comparison table. See DOI: https://doi.org/10.1039/d4ma01249f

© 2025 The Author(s). Published by the Royal Society of Chemistry

Open Access Article. Published on 13 March 2025. Downloaded on 2/2/2026 9:34:04 AM. This article is licensed under a Creative Commons Attribution-NonCommercial 3.0 Unported Licence.

(H_2) is the most plentiful element obtainable from a diverse array of sources such as alcohol and biomass; (iii) the primary benefit of using hydrogen energy is that it produces almost no harmful emissions when burned; and (iv) hydrogen energy is a highly efficient fuel source, outperforming traditional energy sources by producing greater energy per unit of fuel.[7] Following the initial report by Honda and Fujishima on TiO_2 electrodes, significant research has focused on photocatalytic and photoelectrochemical (PEC) water splitting to enhance hydrogen fuel production and support the hydrogen economy.[6] Although TiO_2 has been the most extensively studied photocatalyst to date, its large energy gap of 3.2 eV has limited its ability to effectively utilize sunlight.[6] Given these intrinsic benefits, further research should focus on developing PANI-based composites to enhance photocatalytic materials. Polyaniline (PANI) is a conductive polymer characterized by a delocalized π–π conjugated structure.[8] Its benzenoid and quinonoid units exhibit multiple redox states along with various other intriguing properties. Furthermore, PANI is highly suitable for large-scale applications because of its excellent conductivity, outstanding environmental stability, and ease of preparation.[9] A stable matrix can enhance the durability of the resulting composite.

On the other hand, graphene oxide, with its extensive surface area and unique optical, transport, mechanical, and electronic properties, has become a strong candidate for various applications, including hydrogen production and catalytic activities.[10] It provides a two-dimensional (2D) surface for catalyst deposition and enhances the dye adsorption capacity through π–π interactions between the dye and the aromatic regions of graphene. Moreover, PANI serves as an electron donor and a hole conductor, while graphene functions as an electron acceptor when exposed to visible or UV light.[11] Thus, integrating them with inorganic materials, particularly transition metal oxides or sulfides, enhances the degradation rate by leveraging synergistic effects that reduce recombination losses. The photocatalytic properties of various transition-metal oxides, such as NiO, BiOCl, ZnO, MnO_2, TiO_2, MoO_3, and Cu_2O, have been analyzed.[12–14] An RGO/PANI/Cu_2O hydrogel synthesized by Miao *et al.* demonstrated Congo red degradation within 20 minutes, reflecting an improvement in the composite's performance.[15] Zhang *et al.* showed that a composite of poly(3,4-ethylenedioxythiophene) combined with graphene and MnO_2 exhibited catalytic activity, as it successfully degraded methylene blue (MB) after 7 hours.[16] Pendiselvi *et al.* explored the use of graphitic carbon nitride as a mechanical support, achieving methylene blue (MB) degradation in 80 minutes.[17] Moreover, *in situ* polymerization of aniline with graphene and $ZnFe_2O_4$ results in the formation of a catalyst that greatly enhances the degradation efficiency of rhodamine B.[18] Additionally, the incorporation of gold nanoparticles into a ternary composite with graphene and TiO_2 has been investigated, demonstrating complete methylene blue (MB) degradation after 250 minutes.[19] Additionally, many of these photocatalysts face challenges such as the limited photo response of TiO_2 to visible light, the high expense of Ag or Au used as key components in the composites, and prolonged degradation times. Nevertheless, MoS_2 has a layered configuration characterized by a hexagonal pattern of Mo and S atoms, resulting in S–Mo–S bonding.[20] Furthermore, the layered structure of bulk MoS_2 allows easy intercalation of foreign atoms between its layers.[21] In summary, the combined effect of the ternary composite enhances the nanocomposite's photocatalytic activity, establishing it as a leading photocatalyst.

This study focuses on developing a new ternary composite of polyaniline (PANI), molybdenum disulfide (MoS_2), and graphene oxide (GO) to evaluate its effectiveness in degrading methyl orange (MO) dye through photocatalysis under an LED light. The synthesized composites were thoroughly characterized using XRD, XPS, FTIR, FESEM, and UV-DRS techniques. Various photocatalytic factors, including the catalyst dosage, illuminated area, solution pH, and effect of scavengers, were investigated. Degradation intermediates and final products were analyzed using GC/MS, and possible mechanisms were explored for better understanding. Additionally, the photocatalyst's potential for green hydrogen generation *via* photocatalytic water splitting was assessed under various conditions—sacrificial agent presence and acidic, basic, and neutral environments. The apparent quantum yield (AQE%) for water splitting was also calculated, demonstrating the catalyst's ability to absorb photons and drive chemical reactions that degrade organic pollutants and dissociate water into H_2 and O_2.

2. Experimental section

The chemicals used in the synthesis process are outlined in the ESI† (S1).

2.1. Synthesis of MoS_2 and a ternary nanocomposite

Polyaniline (PANI) and graphene oxide (GO) are synthesized using the oxidative polymerization method and modified Hummers' method, respectively, as outlined in our prior research.[22] For the synthesis of MoS_2, ammonium molybdate tetrahydrate and thiourea were initially dissolved in 20 ml of ethylene glycol; then the mixture was stirred for one hour. The mixture was then sonicated for one hour to ensure complete dispersion of the precursor. Then the prepared solution was heated for 30 minutes at 180 °C temperature in a microwave synthesizer (Biotage initiator $^+$).

A 1 : 1 GO/MoS_2 (wt/wt%) composite was first synthesized using the MoS_2 precursor through an *in situ* method. Next, different weight percentages of the 1 : 1 GO/MoS_2 composite were used to form a ternary composite *via* oxidative polymerization. Initially, 1 : 1 GO/MoS_2 and aniline were combined in a 2 M HCl solution, stirred for one hour, and then sonicated for another hour. Next, ammonium persulfate (APS) was added gradually and the mixture was stirred overnight to facilitate polymerization. The resulting solution was rinsed with 2 M HCl and water and then dried at 60 °C for 24 hours. Thus, the PANI/GO/MoS_2 composites were prepared in different weight ratios (1, 2.5, and 4) and were designated as 1PGMS, 2.5PGMS, and

© 2025 The Author(s). Published by the Royal Society of Chemistry

Open Access Article. Published on 13 March 2025. Downloaded on 2/2/2026 9:34:04 AM. This article is licensed under a Creative Commons Attribution-NonCommercial 3.0 Unported Licence.

4PGMS, respectively. Fig. S1 (ESI†) illustrates the schematic of the synthesis procedure.

2.2. Techniques for characterization

Full details of characterization and the instruments used are found in the ESI† (S2).

2.3. Photocatalysis experiments

2.3.1. Assessment of photocatalytic degradation effectiveness. For photocatalytic degradation assessment, 4 mg of the photocatalyst was mixed with 20 ml of a 20 ppm methyl orange (MO) solution. The mixture was stored in the dark for 120 minutes to achieve equilibrium. Subsequently, the MO solution was exposed to photodegradation under illumination from a 40 W LED lamp in a photocatalytic reactor, with continuous stirring. MO concentrations were monitored using a UV-vis spectrophotometer, and the degradation percentage of MO was determined using the following formula:

$$\text{Degradation } (\%) = \frac{C_0 - C_t}{C_t} \times 100 \quad (1)$$

At the start of the experiment, the concentration of MO is denoted as C_0, while C_t represents the concentration of MO after it has been subjected to light irradiation for a specified period, 't'.

The degree of mineralization was calculated using the following equation:

$$\text{Mineralization } (\%) = \frac{\text{TOC}_{\text{initial}} - \text{TOC}_{\text{final}}}{\text{TOC}_{\text{initial}}} \times 100 \quad (2)$$

In this context, "$\text{TOC}_{\text{initial}}$" refers to the initial concentration of total organic carbon (TOC) in MO, measured in mg L^{-1}, before the degradation process begins. "$\text{TOC}_{\text{final}}$" indicates the TOC concentration in MO after 120 minutes of degradation.

A GC-MS system identified the degradation products of MO, using m/z values to deduce their chemical structures, where 'm' is the molecular mass and 'z' is the charge number. The analysis used aqueous solutions with 0.1% dichloromethane (DCM) as the mobile phase.

2.3.2. Hydrogen production through photocatalysis. A 2 mg photocatalyst was mixed into 20 ml of an aqueous solution containing 1 ml of MeOH as a sacrificial agent. The experiment was performed under four varying conditions: without a sacrificial agent, in an acidic medium, in a basic medium, and with a sacrificial agent in a nitrogen-filled environment. The container was securely closed with an airtight lid. The analysis of the H_2 photoproduct was performed using gas chromatography (GC) with a thermal conductivity detector (TCD), employing nitrogen as the carrier gas. This was conducted in a photocatalytic reactor equipped with a 40 W Philips LED lamp serving as the light source. Throughout the photocatalytic process, a magnetic stirrer was used to keep the system in constant motion. The apparent quantum efficiency (AQE) was calculated using the formula provided below:

$$\text{AQE } (\%) = \frac{n \times \Delta G}{W \times S \times T} \times 100 \quad (3)$$

In this formula, the variables are defined as follows: n represents the moles of hydrogen generated per unit volume (mole per liter); ΔG denotes the total Gibbs free energy for water splitting (237 kJ per mole); W indicates the intensity of light radiation (637 watts per square meter); S refers to the surface region of the reaction vessel (in square meters); and T signifies the reaction time (in seconds).

3. Results and discussion

3.1. Characterization of the synthesized photocatalyst

3.1.1. Analysis of spectral properties. X-ray diffractograms in the 10° to 80° range were used to analyze the phase composition and crystalline structure of the prepared samples (Fig. 1(a)). The XRD analysis reveals peaks at 2θ = 14.92° (121), 20.48° (310), and 25.33° (003), indicating the presence of PANI.[10] The peak at 25.33° (003) particularly highlights the polymeric nature of PANI. Additionally, the presence of graphitic graphene oxide (GO) is evidenced by the peaks observed at 11.23° (002) and 42.16° (100).[23] The diffraction peaks observed at 13.01° and 28.1° (2θ) correspond to the lattice planes (002) and (004) of crystalline MoS_2, respectively, according to JCPDS card no. 65-0160. Analysis of the XRD patterns for the nanocomposites 1PGMS, 2.5PGMS, and 4PGMS shows that peaks attributed to MoS_2, GO, and PANI are still present. This indicates that these components have been effectively integrated into the nanocomposite structures. In the nanocomposite, the broad peak at 2θ = 14.54° could be attributed to the d(121) spacing of PANI, the d(002) spacing of GO, and the d(002) spacing of MoS_2. To calculate the average crystallite sizes of MoS_2, PANI, g-GO, and 2.5PGMS, we employed the Scherrer equation. The Scherrer equation is:[24]

$$D = \frac{k \times \lambda}{\beta \times \cos\theta} \quad (4)$$

The Scherrer equation is used to calculate the crystallite size (D) and depends on several parameters: the Scherrer constant (k), the X-ray source wavelength (λ, usually 0.15406 nm), the full-width half-maxima (β) in radians, and the peak position (θ) also in radians. Using the Scherrer equation with these parameters, the crystallite sizes (D) are determined to be 40.4 nm for MoS_2, 132.21 nm for PANI, 101.6 nm for g-GO, and 108.32 nm for 2.5PGMO.

X-ray photoelectron spectroscopy (XPS) was used to examine the chemical composition and phase state of the synthesized ternary nanocomposite (2.5PGMS). Fig. 2(a) shows the XPS survey spectrum, conclusively confirming the presence of elements Mo, C, N, S, and O within the ternary composite. Gaussian fitting was employed to deconvolute the elemental spectra of Mo 3d, C 1s, N 1s, S 2p, and O 1s, allowing for a more

Open Access Article. Published on 13 March 2025. Downloaded on 2/2/2026 9:34:04 AM.
This article is licensed under a Creative Commons Attribution-NonCommercial 3.0 Unported Licence.

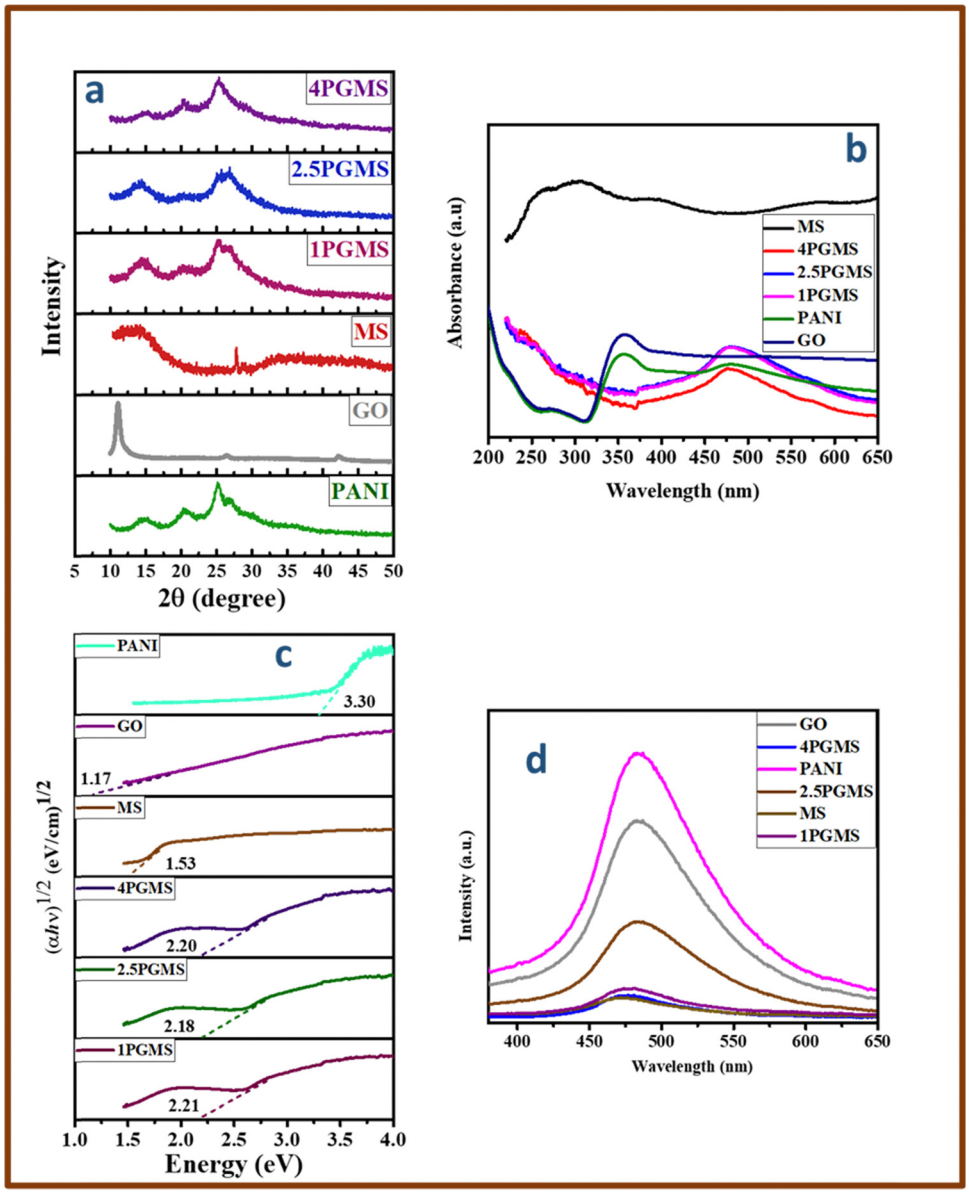

Fig. 1 (a) XRD pattern, (b) UV-vis DRS spectra, (c) Tauc plot, and (d) PL spectra of GO, PANI, MS, 1PGMS, 2.5PGMS, and 4PGMS.

detailed examination of the elemental composition and chemical states. Fig. 2(b) shows the C 1s spectrum with four distinct binding energies. The peak at 283.90 eV corresponds to non-oxygenated carbon, including C–H and C–C bonds. The 284.7 eV peak signifies the presence of graphitic carbon. The 285.5 eV peak indicates nitrogenous carbon, with bonds like C–N. The peak at 288.1 eV corresponds to the C═O bond.[25] Fig. 2(d) displays three distinct peaks in the N 1s spectrum, each corresponding to different nitrogen environments. The peak at 398.8 eV represents quinoid amine, the 399.1 eV peak is linked to benzenoid amine, and the 399.3 eV peak indicates the presence of a nitrogen cationic radical ($N^{+\bullet}$).[26] Fig. 2(c) shows the O 1s spectrum with two main peaks at 531 eV and 532.3 eV. These peaks correspond to the Mo–O bonds in the MoO_3 and hydroxyl groups on the composite's surface, respectively.[27] In the Mo 3d spectrum, two peaks are observed at 232.2 eV and 235.6 eV (Fig. 2(e)). The binding energy 232.2 eV for Mo^{4+} $3d_{3/2}$ and the binding energy 235.6 eV is for the Mo^{6+} oxidation state.[28] The S 2p spectra at 159 eV and 164 eV correspond to $S^{2-}2p_{3/2}$ and $S^{2-}2p_{1/2}$, respectively (Fig. 2(f)). The peak at 159.2 eV is attributed to C–S–H, while the peak at 164.4 eV is assigned to the N–S–H bond.[29] Additionally, a peak at 168.6 eV indicates an S–O bond, indicating partial oxidation of the S edges in MoS_2.[28] From the peak of the S–O bond, we can conclude the formation of a bond between oxygenated graphene oxide and MoS_2. This highlights oxygen's crucial role in the composite's bonding network, contributing to interactions and structural stability.

FTIR analysis identifies distinct absorption peaks linked to specific vibrational modes and chemical groups (Fig. S1, ESI†).

© 2025 The Author(s). Published by the Royal Society of Chemistry

Open Access Article. Published on 13 March 2025. Downloaded on 2/2/2026 9:34:04 AM. This article is licensed under a Creative Commons Attribution-NonCommercial 3.0 Unported Licence.

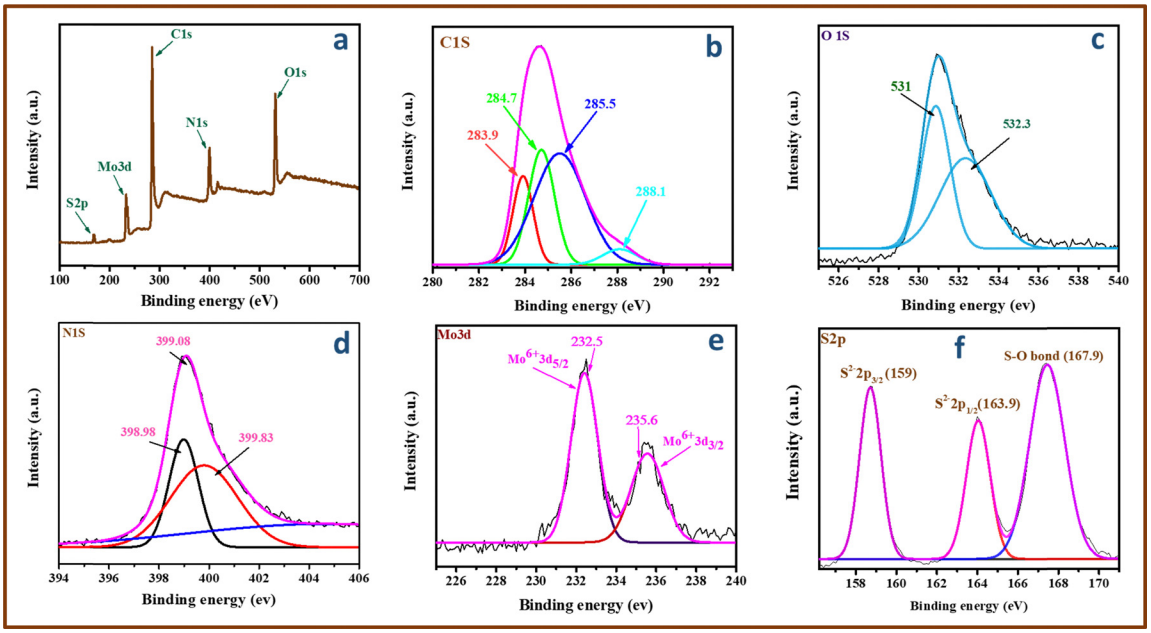

Fig. 2 (a) XPS survey spectrum of 2.5PGMS and core level spectrum of (b) C 1s, (c) O 1s, (d) N 1s, (e) Mo 3d, and (f) S 2p.

The 1536 cm^{-1} peak corresponds to the C=C stretching in the benzenoid ring, while the 1390 cm^{-1} peak indicates the C–N bond stretching. The 1265 cm^{-1} signal reveals the presence of a protonated C–N group.[30,31] Additionally, a peak near 776 cm^{-1} suggests electron delocalization in the polymer matrix. In the graphene oxide (GO) spectrum, distinctive peaks appear. The peak around 3500 cm^{-1} corresponds to O–H bond stretching, while the 1717 cm^{-1} peak indicates C=O stretching in carboxylic groups. The 1615 cm^{-1} peak represents O–H bending and aromatic C=C stretching, and the 1385 cm^{-1} peak suggests the presence of tertiary C–OH bonds.[32–34] Finally, the 1220 cm^{-1} peak confirms the existence of epoxy C–O groups. Broad absorption bands at 501 cm^{-1}, 695 cm^{-1}, and 1623 cm^{-1} are associated with MoS_2.[35] Peaks at 501 cm^{-1} correspond to S–S bonds.[36] Additionally, the band around 3100 cm^{-1} is associated with O–H group vibrations.

A photocatalyst's light absorption capability is essential for its photocatalytic activity. Fig. 1(b) shows the UV-vis absorption spectra of the different as-synthesized photocatalysts. MoS_2 nanospheres absorb strongly in the UV range (250–400 nm), whereas the ternary nanocomposites (PGMS) exhibit wider absorption across the visible spectra. The broader absorption is due to PANI, which sensitizes the photocatalysts to visible light. Additionally, the color change from black in MoS_2 to dark green in the ternary nanocomposites indicates successful PANI integration and enhanced visible light absorption (Fig. 1(b)). Tauc's formula, $(\alpha h\nu)^{(1/n)} = A(h\nu - E_g)$, calculates a semiconductor's energy gap. In this formula, $h\nu$ is the photon energy, E_g is the bandgap, A is a constant, and α is the coefficient of light absorption. The exponent "n" reflects the electronic transition type, where $n = 1/2$ signifies a direct transition. In this study, the bandgap energy (E_g) was determined from plots of $(\alpha h\nu)^{1/2}$ *versus* E_g. As shown in Fig. 1(c), the E_g values are 1.53 eV for MoS_2, 2.18 eV for 2.5PGMS, 2.21 eV for 1PGMS, and 2.20 eV for 4PGMS.

Photoluminescence (PL) spectra are commonly used to evaluate processes like carrier capture, movement, transport, isolation, and recombination. Fig. 1(d) shows the PL emission spectra for MoS_2, PANI, GO, and PGMS composites, highlighting a luminescent peak around 452 nm. Notably, the PL emission intensity of PGMS composites is significantly lower compared to pure MoS_2, PANI, and GO. This reduced fluorescence indicates the potent isolation of light-generated pairs of electrons and holes within the composite structure. Efficient management of electron–hole pairs is crucial for improving photocatalytic degradation. Effective separation of these pairs prevents recombination, allowing for better utilization in photocatalytic reactions.

3.1.2. EIS analysis. EIS measurements were utilized to evaluate the charge transfer efficiency in PANI, GO, MS and their nanocomposite (Fig. S2, ESI†). In a Nyquist plot, a smaller arc radius typically indicates improved interfacial charge transport. The incorporation of PANI, GO, and MS co-catalysts resulted in a reduced arc radius, suggesting lower electron transfer resistance and decreased recombination of electron–hole pairs, ultimately enhancing interfacial charge carrier transport. Among the tested materials, the ternary 2.5PGMS composite exhibited the smallest arc radius, demonstrating its superior conductivity, faster charge migration, and more effective separation of photo-induced carriers. These EIS results are consistent with the PL analysis, underscoring the critical role of the ternary 2.5PGMS hybrid in optimizing charge separation.

3.1.3. Surface properties. FESEM investigation was conducted to understand the arrangement properties of the synthesized composite. FESEM images of MoS_2, PANI, GO, and the 1PGMS composite are depicted in Fig. 3(a–d). The MoS_2 sample

Open Access Article. Published on 13 March 2025. Downloaded on 2/2/2026 9:34:04 AM.
This article is licensed under a Creative Commons Attribution-NonCommercial 3.0 Unported Licence.

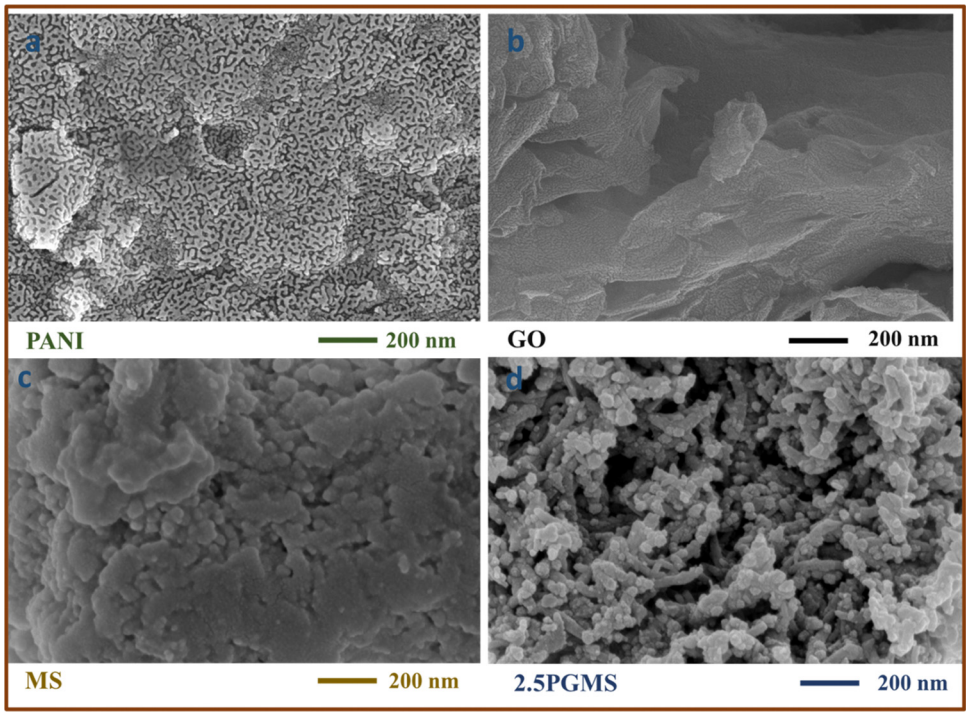

Fig. 3 FESEM images of (a) PANI, (b) GO, (c) MS, and (d) 2.5 PGMS.

exhibited nanospheres ranging from 35 to 55 nm in diameter, while PANI displayed a fibrous, porous morphology. GO's exfoliated and well-agglomerated layers were observed, likely attributable to oxygenated surface functional groups. In the nanocomposite, GO agglomerated with PANI, and MoS_2 nanospheres were visible in the mixture (Fig. 3(d)). The FESEM images confirmed the existence of polyaniline, GO, and MoS_2, indicating the successful establishment of heterojunctions. Energy dispersive spectroscopy (EDS) analysis, shown in Fig. S6 (ESI†), confirmed the presence of C, N, Mo, O, and S in the nanocomposite.

The specific surface area of the synthesized nanocomposites was evaluated to analyze their surface characteristics in detail. Fig. S4 and S5 (ESI†) present the nitrogen adsorption–desorption isotherms, which exhibit a type IV Langmuir isotherm with distinct H1 hysteresis loops for all the composites, as well as for individual components such as MoS_2, PANI, and GO. The presence of these hysteresis loops confirms the mesoporous nature of the materials, indicating well-defined pore structures.

The pore size distribution was determined using the Barrett–Joyner–Halenda (BJH) method, as depicted in Fig. S4 and S5 (ESI†). Table 1 provides a comparative analysis of surface area and pore volume, showing that pure PANI possesses a relatively high surface area and pore volume. However, the synthesized composites exhibit even higher surface areas than pure PANI, GO, and MoS_2, highlighting their enhanced porosity and surface characteristics.

Notably, the PGMS composites follow an increasing trend in surface area, with values recorded as 35.1 $m^2\ g^{-1}$ for 1PGMS, 43 $m^2\ g^{-1}$ for 4PGMS, and 52.6 $m^2\ g^{-1}$ for 2.5PGMS. The superior photocatalytic performance of the 2.5PGMS composite is attributed to its higher surface area, which enhances pollutant adsorption and provides more active sites for catalytic reactions. This increased active surface area plays a crucial role in improving hydrogen production through water splitting, further confirming the composite's effectiveness in photocatalytic applications.

Table 1 BET-specific surface area, total pore volume, and average pore diameter

Photocatalyst	Specific surface area ($m^2\ g^{-1}$)	Total pore volume ($cm^3\ g^{-1}$)	Average pore diameter (nm)
PANI	18.3	0.0203	4.5
GO	10.6	0.034	5.3
MS	7.3	0.0073	4.2
1PGMS	35.1	0.044	5.0
2.5PGMS	52.6	0.0841	6.4
4PGMS	43	0.052	4.8

3.2. Removal of the organic pollutant methyl orange (MO) through photocatalysis

Fig. 4(d) illustrates the limited effectiveness of photolysis alone for removing methyl orange (MO), showing only about a 4% decrease in absorbance after 120 minutes of LED light exposure. This minimal reduction indicates that MO is highly resistant to light-induced degradation. In the dark, after 120 minutes of reaching adsorption–desorption equilibrium, 2.5PGMS adsorbed approximately 32% of MO. In comparison, other materials showed lower adsorption: bare PANI (21%), GO (26%), molybdenum trioxide (9%), 1PG (1 wt% of GO) (12%), 11GMS (1 : 1 of GO and MoS_2) (11%), 1PMS (1 wt% of MoS_2) (10%), 1PGMS (28%),

© 2025 The Author(s). Published by the Royal Society of Chemistry

Open Access Article. Published on 13 March 2025. Downloaded on 2/2/2026 9:34:04 AM. This article is licensed under a Creative Commons Attribution-NonCommercial 3.0 Unported Licence.

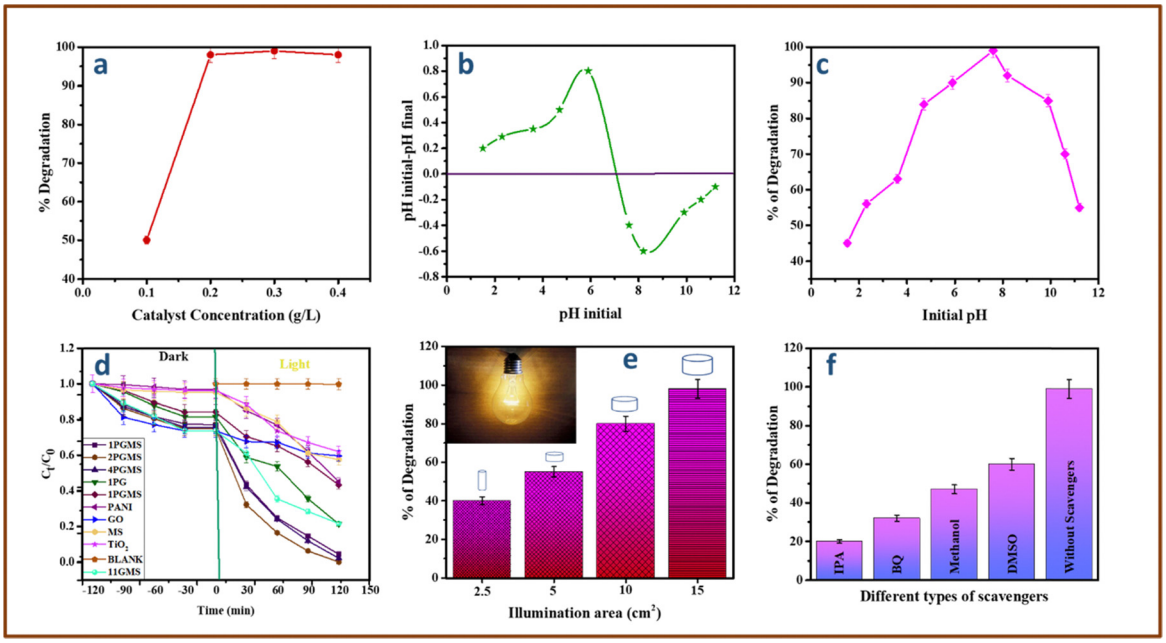

Fig. 4 (a) Effect of catalyst concentration, (b) pzc studies, (c) effect of pH, (d) kinetic studies, (e) impact of illuminated surface area, and (f) scavenger studies.

4PGMS (29%), and TiO_2 (8%) (Fig. 4(d)). The enhanced adsorption capacity of 2.5PGMS is because of the increased surface area and a higher count of adsorption areas for the anionic dye, achieved by incorporating 2.5 wt% GO/MS into PANI. Upon illumination with an LED light for 120 minutes, the photocatalytic efficiency improved as follows: PANI (30%) < GO (32%) < MoS_2 (33%) < TiO_2 (34%) < 1PMS (46%) < 1PG (53%) < 11GMS (74%) < 1PGMS (87%) < 4PGMS (85%) < 2.5PGMS (99%) (Fig. 4(d)). This indicates that bare MoS_2's limited photodegradation capability is due to its restricted photo-response spectrum, inadequate surface area, and rapid recombination of photo-induced charge carriers. PANI and GO improve performance, with 1PMS, 1PG, and 11GMS showing enhanced photocatalytic activity compared to single-component materials. However, increasing 11GMS beyond 2.5 wt% slightly decreased the MO removal efficiency. This reduction is attributed to inefficient charge distribution and potential blocking of active sites by excess 11GMS, which limits light penetration and photocatalytic efficiency. Thus, an optimal 11GMS load maximizes the synergy between PANI, GO, and MoS_2, enhancing photocatalytic activity through a smaller band gap, better light absorption, and reduced recombination of electron–hole pairs. Furthermore, the kinetics of MO photocatalytic degradation were quantitatively analyzed using a pseudo-first-order rate equation on the experimental results:

$$\ln(C_t/C_0) = -kt \quad (5)$$

In this analysis, C_0 and C_t denote the MO concentrations at the start and after t minutes of irradiation, respectively, while k represents the reaction rate constant (min^{-1}). Fig. S7 (ESI†) illustrates the linear correlation between $\ln(C_t/C_0)$ and the reaction time for different catalysts. The degradation rate constants are as follows: 1PGMS (0.02353 min^{-1}), 2.5PGMS (0.03 min^{-1}), 4PGMS (0.02523 min^{-1}), 1PG (0.01241 min^{-1}), 1PMS (0.00512 min^{-1}), 11GMS (0.0123 min^{-1}), PANI (0.00422 min^{-1}), GO (0.00135 min^{-1}), MoS_2 (0.00472 min^{-1}), and TiO_2 (0.00324 min^{-1}). The synergy from combining PANI, GO, and MoS_2 was measured using the synergy factor (R), determined by the equation:

$$R = \frac{K_{PANI+GO+MoS_2}}{K_{PANI} + K_{GO} + K_{MoS_2}} \quad (6)$$

The rate constants for photodegradation of the PANI/GO/MoS_2 composite and individual components (PANI, GO, and MoS_2) are denoted as $K_{(PANI+GO+MoS_2)}$, K_{PANI}, K_{GO}, and K_{MoS_2}, respectively. The synergy factors calculated for 1PGMS, 2.5PGMS, 4PGMS, 1PG, 1PMS, and 11GMS are 1.9, 2.6, 2.3, 1.6, 0.5, and 1.8, respectively. Among these, 2.5PGMS exhibited the highest synergy factor, leading to its most effective photocatalytic degradation with a rate constant of 0.03 min^{-1}.

3.2.1. Effect of the catalyst dosage amount. The efficiency of the photocatalyst is primarily influenced by the amount of catalyst used. To examine how dosage impacts MO degradation, experiments were conducted with varying amounts of the ternary photocatalyst (2.5PGMO) from 1 to 4 mg, keeping the MO concentration constant at 20 ppm. At the lowest dosage (0.1 g L^{-1}), fewer active species were involved in MO degradation, leading to reduced photocatalytic efficiency. The optimal degradation efficiency occurred at 0.2 g L^{-1} (Fig. 4(a)), where active site availability and light energy utilization were maximized. However, increasing the catalyst dosage beyond 0.2 g L^{-1} did not significantly enhance the degradation rate, likely due to catalyst accumulation, which could reduce solution transparency and light

Open Access Article. Published on 13 March 2025. Downloaded on 2/2/2026 9:34:04 AM.
This article is licensed under a Creative Commons Attribution-NonCommercial 3.0 Unported Licence.

penetration, as well as deactivate some catalyst surface areas. These results suggest that 0.2 g L^{-1} is the optimal catalyst dosage for maximum MO photodegradation.

3.2.2. Impact of the solution's pH. The dye solution's pH notably impacts the composite's adsorption ability and thus influences the degradation efficiency.[37] To examine how pH affects the removal of MO dye, solutions with different pH levels were prepared using 0.1 N HCl and 0.1 N NaOH. The pH of the catalyst-to-dye solutions at a concentration of 0.2 g L^{-1} was recorded before and after the degradation process. As shown in Fig. 4(b), the composite 2.5PGMS has a point of zero charge (pzc) around pH 7.07. Degradation efficiency increases from pH 1 to 6, peaking at pH 7.6 (Fig. 4(c)). In basic solutions, the efficiency decreases. These results highlight the critical role of solution pH in controlling the photocatalytic degradation efficiency of the composite. The surface charge of the composite, influenced by pH, plays a key role in the adsorption and degradation of MO dye molecules. Optimal performance is achieved under slightly basic conditions (pH 7.6), stressing the importance of pH in designing effective photocatalytic processes. In strongly alkaline solutions, the formation of metal hydroxide precipitates on the catalyst surface leads to reduced degradation efficiency.

3.2.3. Impact of the lighted area. The research examined the influence of the illuminated surface area on the photocatalytic efficiency of 2.5PGMS when exposed to visible light. A 0.2 g L^{-1} photocatalyst solution mixed with 20 ppm MO dye was agitated for 120 minutes under visible light. Various vessel diameters were employed to alter the reaction surface area, while keeping a consistent distance of 6 cm between the lamp and the surface of the solution. Results showed that increasing the exposed surface area improved degradation efficiency (Fig. 4(e)). Larger surface areas allowed greater light exposure, enhancing photocatalytic degradation and achieving optimal efficiency.

3.2.4. Likely degradation route of MO. To assess the decomposition of organic dyes *via* photodegradation, monitoring TOC and COD levels during light exposure is essential. After 120 minutes of visible light exposure, MO shows a TOC reduction of 83.21% and a COD reduction of 86.11%. Fig. 7(a) indicates nearly complete mineralization, with intermediates having limited mineralization potential, suggesting that the organic dye is broken down into byproducts with reduced mineralization capacity.

The degradation products of MO using the 2.5PGMS nanocomposite were identified through GC-MS analysis. S3 (ESI†) presents the mass spectra for MO degradation by 2.5PGMS. The characteristic mass spectrum of the MO dye is at *m*/*z* 306. After 120 minutes of degradation, the spectra show peaks at *m*/*z* 121, 136, 157, and 172, corresponding to intermediate products. These include sulfanilic acid at *m*/*z* 172, which breaks down into benzenesulfonic acid at *m*/*z* 157 after losing an amino group (NH_2). Similarly, *N*,*N*-dimethyl-*p*-phenylenediamine at *m*/*z* 136 degrades into *N*,*N*-dimethyl benzenenamine at *m*/*z* 121, also after losing an amino group. The results suggest that MO degradation involves cleavage of the azo bond (–N═N–), producing sulfanilic acid and *N*,*N*-dimethyl-*p*-phenylenediamine.[38] The proposed degradation mechanism is shown in Fig. 5, with further breakdown potentially leading to CO_2 and H_2O.

3.2.5. Influence of scavengers on the charge transfer mechanisms. The degradation process mainly relies on electrons from the conduction band (CB), holes in the valence band (VB), as

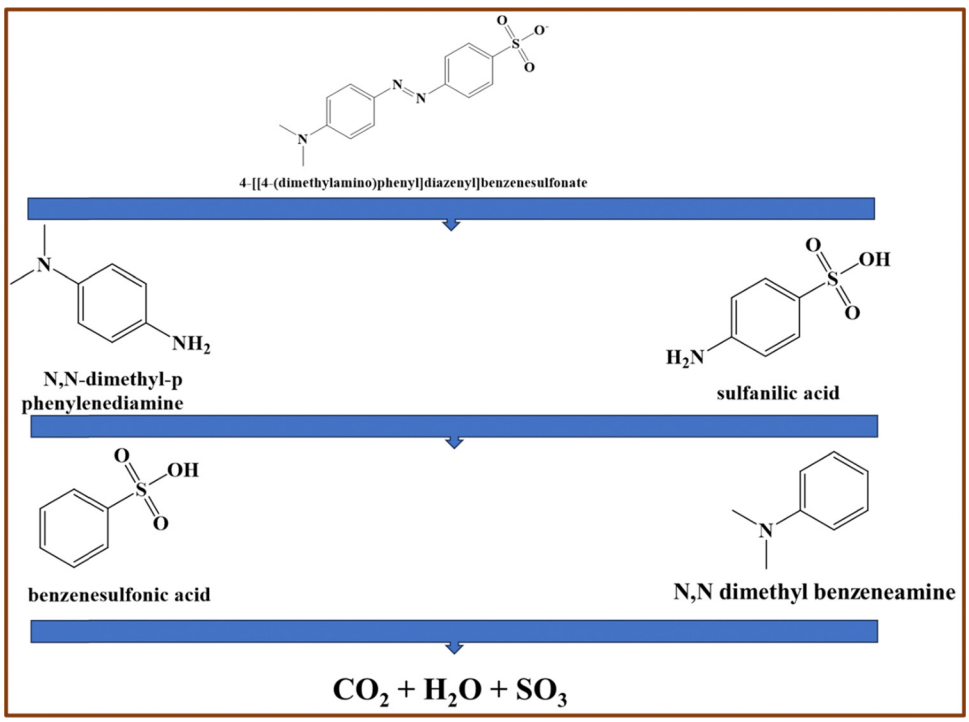

Fig. 5 Proposed mechanism for the photocatalytic breakdown of methyl orange with the 2.5PGMS catalyst.

© 2025 The Author(s). Published by the Royal Society of Chemistry

Open Access Article. Published on 13 March 2025. Downloaded on 2/2/2026 9:34:04 AM. This article is licensed under a Creative Commons Attribution-NonCommercial 3.0 Unported Licence.

well as superoxide and hydroxyl radicals, which play essential roles.[39] A scavenger study was conducted to determine the primary species involved in this process. This study utilized various scavengers, including isopropyl alcohol (IPA), dimethyl sulfoxide (DMSO), benzoquinone (BQ), and methanol, to capture hydroxyl radicals ($OH^{\bullet}$), electrons (e^{-}), superoxide radicals ($O_2^{\bullet-}$), and holes (h^{+}), respectively. The $O_2^{\bullet-}$ radical acts as a reducing agent and interacts with BQ to form hydroquinone.[40] The presence of DMSO highlights the important role of $^{\bullet}OH$ radicals. In DMSO, the unpaired electrons on oxygen atoms facilitate electron transfer and form hydrogen bonds with hydrogen in hydroxyl radicals.[41] As illustrated in Fig. 4(f), methanol, IPA, and BQ play a crucial role in the degradation reaction, underscoring the significance of holes, hydroxyl radicals, and superoxide in the degradation mechanism. The enhanced photocatalytic efficiency of the 2.5PGMS composite results from improved charge separation achieved by integrating GO and MoS_2 within the polyaniline matrix. This effect was explored by analyzing the band positions of MoS_2, GO, and PANI.[42,43] Fig. S3 (ESI†) illustrates the Mott–Schottky plots for PANI, GO, MoS_2, and 2.5PGMS, confirming their characteristic behavior as p-type semiconductors, as indicated by the overall negative slopes. The flat-band potentials, determined from the *x*-axis intersection points of the linear regions, are recorded as −0.349 V for 2.5PGMS, −0.30 V for PANI, 0.21 V for MoS_2, and 0.03 V for GO, all referenced against Ag/AgCl. Notably, the conduction band edge (CB) of the 2.5PGMS composite exhibits a significant negative shift of 0.349 V compared to pure GO and MoS_2. This shift suggests strong electronic interactions among PANI, GO, and MoS_2, resulting in a considerable lowering of the conduction band potential. Consequently, this modification elevates the conduction band to a higher energy level, thereby enhancing the composite's reductive capabilities. The analysis of Mott–Schottky plots and band potential variations provides valuable insights into these electronic interactions, contributing to a better understanding of the improved photocatalytic performance of 2.5PGMS. Photon absorption by GO, MoS_2, and PANI leads to the excitation of electrons into the conduction band (CB) of GO and MoS_2, as well as the lowest unoccupied molecular orbital (LUMO) of PANI. This process simultaneously generates holes in the valence band (VB) of GO and MoS_2 and the highest occupied molecular orbital (HOMO) of PANI. Due to energy minimization tendencies, electrons from the CB of GO and MoS_2 preferentially migrate toward the LUMO of PANI rather than returning to the valence band of GO or MoS_2 *via* the heterojunction barrier. Fig. 6 indicates that when the 2.5PGMS composite is exposed to visible light, PANI gets excited, producing light-induced electrons (e^{-}) and holes (h^{+}). The electrons from PANI's conduction band (CB) move to the conduction bands of GO and MoS_2, which lowers the rate of electron–hole recombination. This decreases the rate of recombination between electrons and holes. Both GO and MoS_2 exhibit higher reduction potentials compared to $O_2/O^{2-\bullet}$ (0.07 eV).[44] Electrons located at the surface of GO and MoS_2 can react with dissolved oxygen molecules, generating superoxide radical anions (O_2/OH_2). Given that the oxidation potential of $H_2O/OH^{\bullet}$

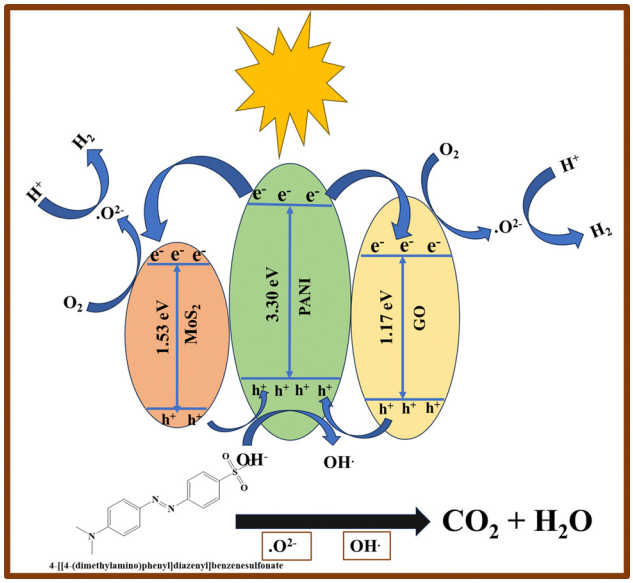

Fig. 6 Proposed charge transfer mechanism for photocatalytic degradation and hydrogen production in the 2.5PGMS composite.

(+2.32 eV) is higher than the valence band of PANI,[44] water molecules can react with holes in the valence band of PANI, leading to the formation of hydroxyl radicals ($OH^{\bullet}$). The proposed methyl orange degradation mechanism is outlined in Fig. 6, along with the corresponding equations (7)–(12).[45]

$$\text{PANI} + h\nu \rightarrow e_{VB}^{-}\,(\text{PANI}) + h_{CB}^{+}\,(\text{PANI}) \quad (7)$$

$$\text{GO} + h\nu \rightarrow e_{CB}^{-}\,(\text{GO}) + h_{VB}^{+}\,(\text{GO}) \quad (8)$$

$$MoS_2 + h\nu \rightarrow e_{CB}^{-}\,(MoS_2) + h_{VB}^{+}\,(MoO_3) \quad (9)$$

$$e_{VB}^{-}\,(\text{PANI}) + O_2 \rightarrow O^{2\bullet-}\,(\text{PANI}) \quad (10)$$

$$h_{VB} + (\text{PANI/GO/MoS}_2) + OH^{-} \rightarrow OH^{\bullet}\,(\text{PANI/GO/MoS}_2) \quad (11)$$

$$O^{2\bullet-}\,(\text{PANI}), OH^{\bullet}\,(\text{PANI/GO/MoS}_2) + \text{MO} \rightarrow \text{Degraded products} \quad (12)$$

3.2.6. Studies on reusability. The durability of a photocatalyst is essential for its continued application in environmental cleanup. Therefore, it's important to assess the composite's stability across multiple photodegradation cycles. The 2.5PGMS composite displayed impressive photostability, maintaining a high degradation efficiency of 85–98% for MO even after five cycles, as shown in Fig. 7(b). XRD analysis after degradation indicated only a slight reduction in peak intensity, likely caused by dye adsorption on the catalyst's surface, while the XRD pattern remained unchanged (Fig. 7(c)). These findings suggest that the photocatalyst retains its durability and structural integrity over time. The 2.5PGMS photocatalyst was systematically compared with various materials documented in the literature for their efficacy in photocatalytic detoxification of organic pollutants, as detailed in Table S2 (ESI†). This comparative analysis reveals that 2.5PGMS not only achieves superior degradation

Open Access Article. Published on 13 March 2025. Downloaded on 2/2/2026 9:34:04 AM.
This article is licensed under a Creative Commons Attribution-NonCommercial 3.0 Unported Licence.

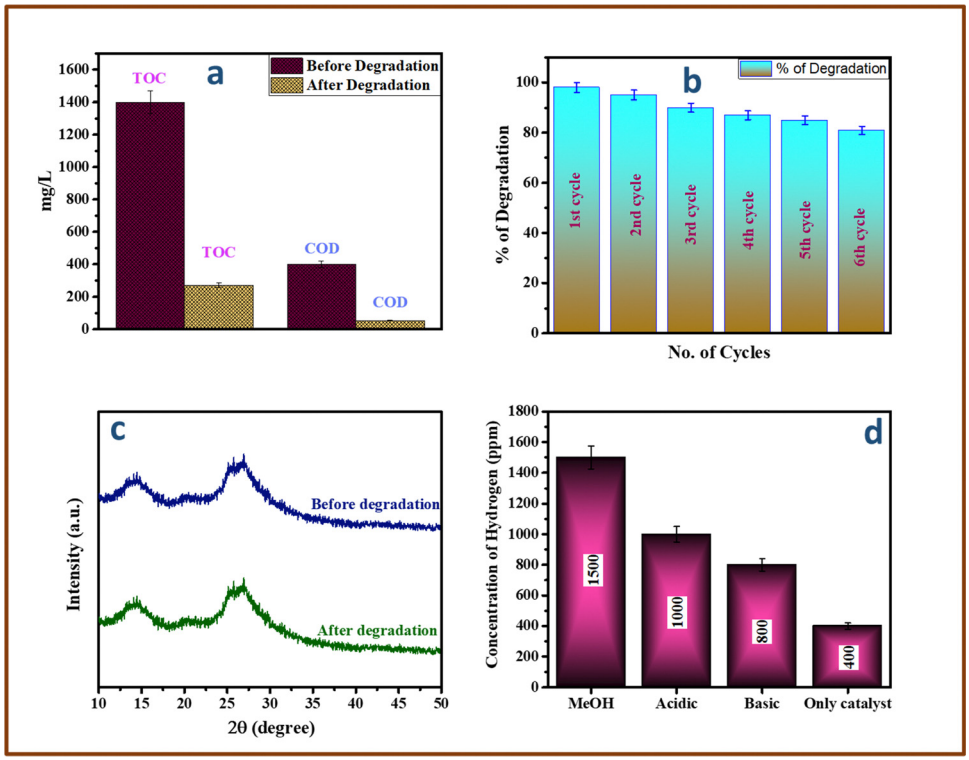

Fig. 7 (a) TOC and COD of MO before and after degradation, (b) reusability studies, (c) XRD of 2.5PGMS before and after degradation, and (d) hydrogen production studies.

efficiency but also does so at a lower catalyst concentration, highlighting its potential in effectively treating persistent organic pollutants with enhanced efficiency and reduced material usage.

3.2.7. Studies on hydrogen production *via* photocatalysis. Hydrogen generation through photocatalytic water splitting was studied over 24 hours under an LED light using four different solutions. The first solution included 1 ml of methanol (sacrificial agent) in 19 ml of water. The second solution consisted of 1 ml of HCl diluted in 19 ml of water, while the third was basic, comprising 1 ml of 1N NaOH mixed with 19 ml of water. The fourth solution contained only 20 ml of water. In the presence of methanol, 1500 ppm of hydrogen gas was generated (Fig. 7(d)). Methanol serves as a sacrificial donor and hole scavenger, leading to the formation of intermediates like formaldehyde or formic acid. In the photocatalytic reaction, hydrogen ions (H^+) partially participate in the reduction process with these intermediates. Hydrogen production reached 1000 ppm under acidic conditions, whereas under basic conditions, it is 800 ppm (Fig. 7(d)). With just the catalyst and water, 400 ppm of hydrogen was released (Fig. 7(d)). Quantum efficiency was about 26% with methanol, 22% in acidic solution, 19% in basic solution, and 15% with only the catalyst. Eqn (13)–(16) demonstrate the role of electron–hole pairs in the conduction and valence bands in facilitating redox reactions.[46,47]

Under acidic conditions:

$$\text{Oxidation: } 2H_2O\ (l) + 4h^+ \rightarrow O_2\ (g) + 4H^+\ (aq) \quad E^0\ (\text{oxidation}) = -1.23\ \text{V} \tag{13}$$

$$\text{Reduction: } 2H^+ + 2e^- \rightarrow O_2\ (g) + 2H_2\ (g) \quad E^0\ \text{reduction} = 0\ \text{V}. \tag{14}$$

Under basic conditions:

$$\text{Oxidation: } 2OH^-\ (aq) \rightarrow 1/2\ O_2\ (g) + H_2O\ (l) + 2e^- \tag{15}$$

$$\text{Reduction: } 2H_2O\ (l) + 2e^- \rightarrow H_2\ (g) + 2OH^- \tag{16}$$

4. Conclusion

Ternary nanocomposites (PANI/GO/MoS_2) were prepared through *in situ* oxidative polymerization, varying the ratios of GO to MoS_2. Characterization validated the successful synthesis of pure PANI, GO, MoS_2, and their corresponding composites. These materials were utilized for the mineralization of MO and photocatalytic water splitting, employing a sacrificial agent under acidic and basic conditions, as well as with the catalyst on its own. The composite's photocatalytic efficiency under visible light was significantly enhanced by the synergistic interaction among MoS_2, PANI, and GO, with 2.5PGMS exhibiting the greatest catalytic activity. Its first-order rate constant (0.03 min^{-1}) was 7.1 times higher than that of PANI, 22 times higher than that of GO, 6.35 times higher than that of MoS_2, and 9.26 times higher than that of TiO_2-P25. Key parameters like the catalyst concentration (0.2 g L^{-1}), illuminated area (15 cm^2), and solution pH (7.6) were investigated for their impact on photodegradation,

© 2025 The Author(s). Published by the Royal Society of Chemistry

Open Access Article. Published on 13 March 2025. Downloaded on 2/2/2026 9:34:04 AM. This article is licensed under a Creative Commons Attribution-NonCommercial 3.0 Unported Licence.

highlighting the importance of h^+, $OH^\bullet$, and $O^{2\bullet}$ in the process. The findings demonstrate that a small amount of photocatalyst (0.2 g L^{-1}) achieves 83.21% detoxification of the MO solution. The apparent quantum efficiency (AQE) for hydrogen production was 26% with CH_3OH as the sacrificial agent, 22% under acidic conditions, 19% under basic conditions, and 15% using only the catalyst. This research showcases PANI/GO/MoS_2 as a potential ternary composite suitable for a range of solar-powered applications.

Author contributions

Pritam Hait: visualization and writing – original draft. Rajeev Mehta: supervision. Soumen Basu: supervision.

Data availability

The data supporting the findings of this study are available from the corresponding author upon reasonable request.

Conflicts of interest

The authors have disclosed that they have no conflicts of interest regarding the conduct of this study and the publication of its findings.

Acknowledgements

We gratefully acknowledge the fellowship funding provided by the TIET-Virginia Tech Center of Excellence in Emerging Materials, India. We also extend our gratitude to DCBC and DPMS TIET for providing us characterization facility, and we are also thankful to Dr Akansha Mehta for XPS characterization. We also want to acknowledge Prof. O. P. Pandey and Mr Abhishek Chandel from DPMS, TIET, Patiala, Punjab for EIS analysis.

References

1 J. Willkomm, K. L. Orchard, A. Reynal, E. Pastor, J. R. Durrant and E. Reisner, *Chem. Soc. Rev.*, 2016, **45**, 9–23.
2 S. Cao, J. Low, J. Yu and M. Jaroniec, *Adv. Mater.*, 2015, **27**, 2150–2176.
3 S. Wang, C. Liu, K. Dai, P. Cai, H. Chen, C. Yang and Q. Huang, *J. Mater. Chem. A*, 2015, **3**, 21090–21098.
4 J. Abdi, M. Vossoughi, N. M. Mahmoodi and I. Alemzadeh, *Chem. Eng. J.*, 2017, **326**, 1145–1158.
5 M. J. Kang and Y. S. Kang, *MRS Adv.*, 2018, **3**, 3271–3280.
6 K. Yan and G. Wu, *ACS Sustainable Chem. Eng.*, 2015, **3**, 779–791.
7 M.-Y. Qi, M. Conte, M. Anpo, Z.-R. Tang and Y.-J. Xu, *Chem. Rev.*, 2021, **121**, 13051–13085.
8 G. Yu, J. Gao, J. C. Hummelen, F. Wudl and A. J. Heeger, *Science*, 1995, **270**, 1789–1791.
9 K. Vinodgopal, D. E. Wynkoop and P. V. Kamat, *Environ. Sci. Technol.*, 1996, **30**, 1660–1666.
10 P. Ahuja, S. K. Ujjain, I. Arora and M. Samim, *ACS Omega*, 2018, **3**, 7846–7855.
11 H. Yang, X. Liu, S. Sun, Y. Nie, H. Wu, T. Yang, S. Zheng and S. Lin, *Mater. Res. Bull.*, 2016, **78**, 112–118.
12 W. Zhang, X. Li, Z. Yang, X. Tang, Y. Ma, M. Li, N. Hu, H. Wei and Y. Zhang, *Nanotechnology*, 2016, **27**, 265703.
13 E. Pajootan, M. Arami and M. Rahimdokht, *Ind. Eng. Chem. Res.*, 2014, **53**, 16261–16269.
14 P. Raizada, P. Singh, A. Kumar, G. Sharma, B. Pare, S. B. Jonnalagadda and P. Thakur, *Appl. Catal., A*, 2014, **486**, 159–169.
15 J. Miao, A. Xie, S. Li, F. Huang, J. Cao and Y. Shen, *Appl. Surf. Sci.*, 2016, **360**, 594–600.
16 N. B. Grimm, S. H. Faeth, N. E. Golubiewski, C. L. Redman, J. Wu, X. Bai and J. M. Briggs, *Science*, 2008, **319**, 756–760.
17 K. Pandiselvi, H. Fang, X. Huang, J. Wang, X. Xu and T. Li, *J. Hazard. Mater.*, 2016, **314**, 67–77.
18 J. Feng, Y. Hou, X. Wang, W. Quan, J. Zhang, Y. Wang and L. Li, *J. Alloys Compd.*, 2016, **681**, 157–166.
19 Y. Yang, Z. Ma, L. Xu, H. Wang and N. Fu, *Appl. Surf. Sci.*, 2016, **369**, 576–583.
20 N. Huo, Y. Yang, Y.-N. Wu, X.-G. Zhang, S. T. Pantelides and G. Konstantatos, *Nanoscale*, 2018, **10**, 15071–15077.
21 T. H. M. Lau, X. Lu, J. Kulhavý, S. Wu, L. Lu, T.-S. Wu, R. Kato, J. S. Foord, Y.-L. Soo, K. Suenaga and S. C. E. Tsang, *Chem. Sci.*, 2018, **9**, 4769–4776.
22 P. Hait, R. Mehta and S. Basu, *J. Cleaner Prod.*, 2023, **424**, 138851.
23 H. Shin, K. K. Kim, A. Benayad, S. Yoon, H. K. Park, I. Jung, M. H. Jin, H. Jeong, J. M. Kim, J. Choi and Y. H. Lee, *Adv. Funct. Mater.*, 2009, **19**, 1987–1992.
24 H. Neelamkodan, U. Megha and P. M. Binitha, *Process. Appl. Ceram.*, 2023, **17**, 149–156.
25 H. Liu, Y. Su, Z. Chen, Z. Jin and Y. Wang, *J. Hazard. Mater.*, 2014, **266**, 75–83.
26 K. Zhang, L. L. Zhang, X. S. Zhao and J. Wu, *Chem. Mater.*, 2010, **22**, 1392–1401.
27 Z. Liu, W. Xu, J. Fang, X. Xu, S. Wu, X. Zhu and Z. Chen, *Appl. Surf. Sci.*, 2012, **259**, 441–447.
28 B. Li, L. Jiang, X. Li, P. Ran, P. Zuo, A. Wang, L. Qu, Y. Zhao, Z. Cheng and Y. Lu, *Sci. Rep.*, 2017, **7**, 11182.
29 H. Wang, M. Thangamuthu, Z. Wu, J. Yang, H. Yuan, M. K. Bayazit and J. Tang, *Chem. Eng. J.*, 2022, **445**, 136790.
30 A. Abdolahi, E. Hamzah, Z. Ibrahim and S. Hashim, *Materials*, 2012, **5**, 1487–1494.
31 G. Gaikwad, P. Patil, D. Patil and J. Naik, *Mater. Sci. Eng. B*, 2017, **218**, 14–22.
32 T. Szabó, E. Tombácz, E. Illés and I. Dékány, *Carbon*, 2006, **44**, 537–545.
33 Y. Fu and X. Wang, *Ind. Eng. Chem. Res.*, 2011, **50**, 7210–7218.
34 Q. Wang, J. Hui, J. Li, Y. Cai, S. Yin, F. Wang and B. Su, *Appl. Surf. Sci.*, 2013, **283**, 577–583.
35 W. Feng, L. Chen, M. Qin, X. Zhou, Q. Zhang, Y. Miao, K. Qiu, Y. Zhang and C. He, *Sci. Rep.*, 2015, **5**, 17422.
36 S. Reshmi, M. V. Akshaya, B. Satpati, A. Roy, P. Kumar Basu and K. Bhattacharjee, *Mater. Res. Express*, 2017, **4**, 115012.

© 2025 The Author(s). Published by the Royal Society of Chemistry

Open Access Article. Published on 13 March 2025. Downloaded on 2/2/2026 9:34:04 AM.
This article is licensed under a Creative Commons Attribution-NonCommercial 3.0 Unported Licence.

37 A. Kumar, R. Kumar and G. Pandey, *Macromol. Symp.*, 2018, **379**(1), 1600192.
38 M. Kgatle, K. Sikhwivhilu, G. Ndlovu and N. Moloto, *Catalysts*, 2021, **11**, 428.
39 A. Kundu, S. Sharma and S. Basu, *J. Phys. Chem. Solids*, 2021, **154**, 110064.
40 S. Singla, S. Sharma and S. Basu, *J. Cleaner Prod.*, 2021, **324**, 129290.
41 H. Alamgholiloo, E. Asgari, S. Nazari, A. Sheikhmohammadi, N. Noroozi Pesyan and B. Hashemzadeh, *Sep. Purif. Technol.*, 2022, **300**, 121911.
42 T. Guo, L. Wang, D. G. Evans and W. Yang, *J. Phys. Chem. C*, 2010, **114**, 4765–4772.
43 T. Lv, L. Pan, X. Liu, T. Lu, G. Zhu and Z. Sun, *J. Alloys Compd.*, 2011, **509**, 10086–10091.
44 P. S. Rao and E. Hayon, *J. Phys. Chem.*, 1975, **79**, 397–402.
45 M. Mitra, S. T. Ahamed, A. Ghosh, A. Mondal, K. Kargupta, S. Ganguly and D. Banerjee, *ACS Omega*, 2019, **4**, 1623–1635.
46 T. Jafari, E. Moharreri, A. Amin, R. Miao, W. Song and S. Suib, *Molecules*, 2016, **21**, 900.
47 A. A. Murashkina, T. V. Bakiev, Y. M. Artemev, A. V. Rudakova, A. V. Emeline and D. W. Bahnemann, *Catalysts*, 2019, **9**, 999.

© 2025 The Author(s). Published by the Royal Society of Chemistry